Effect of Processing on Structure and Ionic Conductivity of Chlorine-Rich Lithium Argyrodites

Wang, Shuo; Gautam, A.; Wu, Xinbin; Li, Shenghao; Zhang, Xin; He, Hongcai; Lin, Yuanhua; Shen, Yang; Nan, Ce Wen

DOI
10.1002/aesr.202200197

Publication date
2024

Document Version
Final published version

Published in
Advanced Energy and Sustainability Research

Citation (APA)
Wang, S., Gautam, A., Wu, X., Li, S., Zhang, X., He, H., Lin, Y., Shen, Y., & Nan, C. W. (2024). Effect of Processing on Structure and Ionic Conductivity of Chlorine-Rich Lithium Argyrodites. *Advanced Energy and Sustainability Research*, *5*(8), Article 2200197. https://doi.org/10.1002/aesr.202200197

Effect of Processing on Structure and Ionic Conductivity of Chlorine-Rich Lithium Argyrodites

Shuo Wang, Ajay Gautam, Xinbin Wu, Shenghao Li, Xin Zhang, Hongcai He, Yuanhua Lin, Yang Shen, and Ce-Wen Nan**

Lithium argyrodite solid electrolytes have attracted ever-increasing attention for all-solid-state batteries due to their high ionic conductivity and low cost. However, the relation between structure and ionic transport for the halogen-rich lithium argyrodites under different synthesis routes is still elusive. Herein, the influence of synthesis procedures, such as annealing conditions and balling milling, on the structure, ionic conductivity, and activation energy of the lithium argyrodite (e.g., $Li_{5.5}PS_{4.5}Cl_{1.5}$, $Li_{5.3}PS_{4.3}Cl_{1.7}$), is systematically investigated. Compared with high-energy ball milling followed by annealing, using fast dry mixing followed by annealing can obtain comparable ionic conductivity of the chlorine-rich lithium argyrodites. Single-crystal $LiNi_{0.83}Co_{0.11}Mn_{0.06}O_2$-based solid-state battery with these electrolytes shows stable cycling performance, demonstrating that chlorine-rich lithium argyrodite is a promising candidate for all-solid-state batteries.

1. Introduction

All-solid-state batteries (ASSBs) with nonflammable solid electrolytes (SEs) are expected to improve the safety and specific energy compared with commercial lithium-ion batteries with liquid electrolytes.[1–3] To reach comparable electrochemical performance with commercial lithium-ion batteries, the ionic conductivity of SEs should be higher than 10^{-2} S cm^{-1} to meet the requirement of sufficient ionic transport especially in the composite cathodes.[4] Among different kinds of superionic conductors, sulfide SEs have aroused great interest due to their high ionic conductivity, good ductility, and easy processing.[5–7] Through decades of effort, the ionic conductivity of sulfide SEs has reached a milestone, such as $Li_{10}GeP_2S_{12}$ (12 mS cm^{-1})[8] and $Li_{6.6}Si_{0.6}Sb_{0.4}S_5I$ (14.8 mS cm^{-1}),[9] which is comparable to that for liquid electrolytes. However, the high-cost Ge element and poor interface stability against cathode active materials or lithium anode still hinder their applications.[10,11]

Lithium argyrodites, such as Li_6PS_5X ($X =$ Cl, Br), due to their high ionic conductivity (10^{-3}–10^{-2} S cm^{-1}) and inexpensive precursors exhibit great potential for ASSBs.[12,13] For example, Li_6PS_5Cl with a high ionic conductivity of about 3.15 mS cm^{-1} was prepared via fast annealing.[14] Theoretical calculations predicted that the Li_6PS_5Cl electrolyte exhibits the highest ionic conductivity when Cl occupies 75% of the 4*d* site, but actually this is difficult to be achieved for Li_6PS_5Cl electrolyte. Therefore, excessive Cl may increase the Cl occupancy in the 4*d* site.[15] Nazar et al. developed a lithium-deficient chlorine-rich $Li_{5.5}PS_{4.5}Cl_{1.5}$ electrolyte with an ultrahigh ionic conductivity of 9.4 mS cm^{-1} via ball milling followed by annealing.[16] The increase of ionic conductivity is due to enlarging S^{2-}/Cl^{-} disorder and weakening the interaction between Li^+ and S^{2-}/Cl^{-}.

Recently, other groups have also prepared several chorine-rich lithium argyrodites (e.g., $Li_{5.5}PS_{4.5}Cl_{1.5}$ and $Li_{5.3}PS_{4.3}Cl_{1.7}$) with high ionic conductivity in the range of 6.4–10.2 mS cm^{-1} via ball milling followed by annealing.[17–21] For example, Gautam et al.

S. Wang, S. Li, X. Zhang
Center of Smart Materials and Devices
State Key Laboratory of Advanced Technology for Materials Synthesis and Processing
School of Material Science and Engineering
Wuhan University of Technology
Wuhan 430070, China
E-mail: shuowang@whut.edu.cn

The ORCID identification number(s) for the author(s) of this article can be found under https://doi.org/10.1002/aesr.202200197.

DOI: 10.1002/aesr.202200197

S. Wang, X. Wu, Y. Lin, Y. Shen, C.-W. Nan
State Key Laboratory of New Ceramics and Fine Processing
School of Materials Science and Engineering
Tsinghua University
Beijing 100084, China
E-mail: cwnan@mail.tsinghua.edu.cn

S. Wang
Foshan (Southern China) Institute for New Materials
Foshan 528200, China

A. Gautam
Department of Radiation Science and Technology
Delft University of Technology
2629 JB Delft, Netherlands

H. He
Qingtao Research Institute
Qingtao Energy Development Inc.
Kunshan 215300, China

prepared $Li_{5.5}PS_{4.5}Cl_{1.5}$ with a high ionic conductivity of 7.2 mS cm^{-1} by mechanical alloying followed by heat-treatment method.[18] Liu et al. also obtained $Li_{5.5}PS_{4.5}Cl_{1.5}$ with a high ionic conductivity of 8 mS cm^{-1} by regulating the annealing temperature of the samples after ball milling.[19] Considering high-energy ball milling is time-consuming and has low repeatability. Peng et al. synthesized an $Li_{5.3}PS_{4.3}Cl_{1.7}$ pellet with an ultrahigh ionic conductivity of 17 mS cm^{-1} via two-step annealing.[22] Similarly, $Li_{5.5}PS_{4.5}Cl_{1.5}$ with a high ionic conductivity of 9.03 mS cm^{-1} (cold-pressing) was prepared by the simple solid-state reaction on the premixed precursors.[23]

Many literatures on $Li_{6-x}PS_{5-x}Cl_{1+x}$ $(0 \leq x \leq 1)$ SEs focus on revealing the ionic transport mechanism by tailoring the halogen content.[16,17,22] However, systematical investigations on the influence of annealing conditions on the ionic transport and phase transition of the chlorine-rich lithium argyrodites have been rarely reported yet. Moreover, several kinds of chlorine-rich lithium argyrodites have been utilized in ASSBs to demonstrate that they are good candidates for ASSBs.[17,19,23] However, the assessment of electrochemical performance of chlorine-rich lithium argyrodites-based ASSBs with ultrahigh-nickel cathodes (nickel content > 80%) has been rarely investigated.

In this study, we systematically investigate the evolution of structure, ionic conductivity, and activation energy of chlorine-rich lithium argyrodites under different synthesis routes, such as with/without mechanical alloying reactions, and various annealing conditions. Our results show that the ionic conductivity of $Li_{5.5}PS_{4.5}Cl_{1.5}$ and $Li_{5.3}PS_{4.3}Cl_{1.7}$ SEs prepared via high-energy ball milling is similar to those of the electrolytes synthesized via fast dry mixing followed by annealing. The ASSB with single-crystal $LiNi_{0.83}Co_{0.11}Mn_{0.06}O_2@Li_3BO_3$ and $Li_{5.5}PS_{4.5}Cl_{1.5}$ as composite cathode, $Li_{5.5}PS_{4.5}Cl_{1.5}$ as solid electrolyte, and In/InLi as anode (i.e., In/InLi | $Li_{5.5}PS_{4.5}Cl_{1.5}$ | s-NCM83(coated)-$Li_{5.5}PS_{4.5}Cl_{1.5}$ cells) offers a stable specific capacity of 158 mAh g^{-1} at 0.2 mA cm^{-2} after 80 cycles. These results demonstrate that chlorine-rich lithium argyrodite has great potential used in ASSBs.

2. Results and Discussion

Two routes were used to prepare the $Li_{5.5}PS_{4.5}Cl_{1.5}$ and $Li_{5.3}PS_{4.3}Cl_{1.7}$ SEs. One is high-energy ball milling followed by annealing (denoted as BA samples), and another is fast dry mixing followed by annealing (denoted as DA samples), as shown in **Figure 1**.

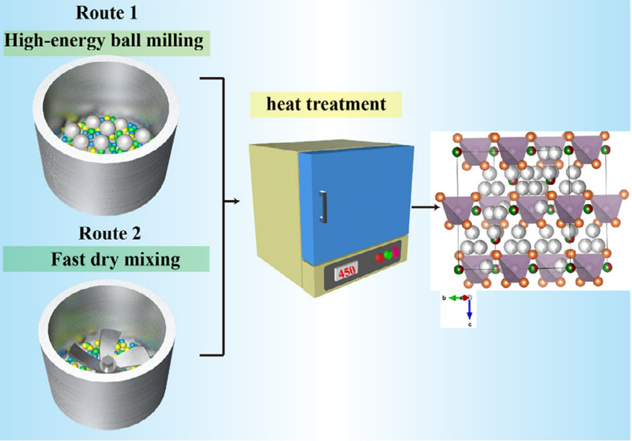

Figure 1. Schematic diagram of two synthesis routes for halogen-rich lithium argytodite $Li_{6-x}PS_{5-x}Cl_{1+x}$ $(0 < x \leq 0.7)$, including high-energy ball milling at 520 rpm for 16 h followed by annealing and fast dry mixing at 18 000 rpm for 3 min followed by heat treatment. The crystal structure of $Li_{6-x}PS_{5-x}Cl_{1+x}$.[18]

Figure 2a shows the X-ray diffraction (XRD) patterns of the BA-$Li_{5.5}PS_{4.5}Cl_{1.5}$ samples annealed at different temperature for 3 h. The corresponding Rietveld refinement and phase composition proportion results are shown in Figure S1 and S4a, Supporting Information, respectively. As for the ball-milling sample without annealing, apart from the main peaks indexed to the $Li_{5.5}PS_{4.5}Cl_{1.5}$ phase, small amount of Li_2S and LiCl impurities also exist. After annealing at 350 °C for 3 h, the content of $Li_{5.5}PS_{4.5}Cl_{1.5}$ increases and the LiCl content diminishes. Meanwhile, the Li_2S impurity disappears and a new $Li_{15}P_4S_{16}Cl_3$ impurity phase appears.[24] When the annealing temperature increases to 450 °C, the LiCl and $Li_{15}P_4S_{16}Cl_3$ impurities disappear and a pure $Li_{5.5}PS_{4.5}Cl_{1.5}$ is obtained. Further increasing the annealing temperature to 500 °C, the LiCl impurity reappears and $Li_{5.5}PS_{4.5}Cl_{1.5}$ with two different lithium argyrodite phases form. This is due to the fact that increasing temperature above the melting, as previous study suggested,[18] results in the formation of lithium argyrodite with different Cl contents, which leads to different lattice volume. Thus, it is possible that one phase is chloride-enriched lithium argyrodite and the other is chloride deficient. The LiCl impurity continues to increase until the temperature reaches 550 °C.

The XRD patterns of the DA-$Li_{5.5}PS_{4.5}Cl_{1.5}$ samples annealed at different temperature for 3 h are shown in Figure 2b. The corresponding Rietveld refinement and phase composition proportion results are shown in Figure S2 and S4b, Supporting Information, respectively. It is noteworthy that the phase evolution tendency of DA-$Li_{5.5}PS_{4.5}Cl_{1.5}$ samples is similar to that of the BA-$Li_{5.5}PS_{4.5}Cl_{1.5}$ samples. Thus, 450 °C is the optimal annealing temperature for obtaining pure $Li_{5.5}PS_{4.5}Cl_{1.5}$ phase for both the BA-$Li_{5.5}PS_{4.5}Cl_{1.5}$ and DA-$Li_{5.5}PS_{4.5}Cl_{1.5}$ samples.

The XRD results of the BA-$Li_{5.5}PS_{4.5}Cl_{1.5}$ samples annealed at 450 °C for various durations are shown in Figure 2c, S1 and S4c, Supporting Information. When the annealing duration prolongs from 1 min to 6 h, pure $Li_{5.5}PS_{4.5}Cl_{1.5}$ phase is obtained without any impurities. As the duration increases to 10 h, beyond the $Li_{5.5}PS_{4.5}Cl_{1.5}$ phase, LiCl impurity phase appears. Further increasing the duration to 24 h, the LiCl content continues to increase. From the XRD results of the DA-$Li_{5.5}PS_{4.5}Cl_{1.5}$ samples annealed at 450 °C for various durations (Figure 2d, S2 and S4d, Supporting Information), it can be observed that all the samples consist of pure $Li_{5.5}PS_{4.5}Cl_{1.5}$ phase.

Figure 2e, S3 and S4e, Supporting Information, shows XRD results of the BA-$Li_{5.3}PS_{4.3}Cl_{1.7}$ samples annealed at different temperatures for 6 h. As for the 390-6h sample, the main peaks are indexed to $Li_{5.3}PS_{4.3}Cl_{1.7}$ phase, and minor peaks are attributed to $Li_{15}P_4S_{16}Cl_3$ and LiCl impurities. As the annealing temperature increases, these impurities content decrease and reach minimum at 430 °C. When the temperature reaches

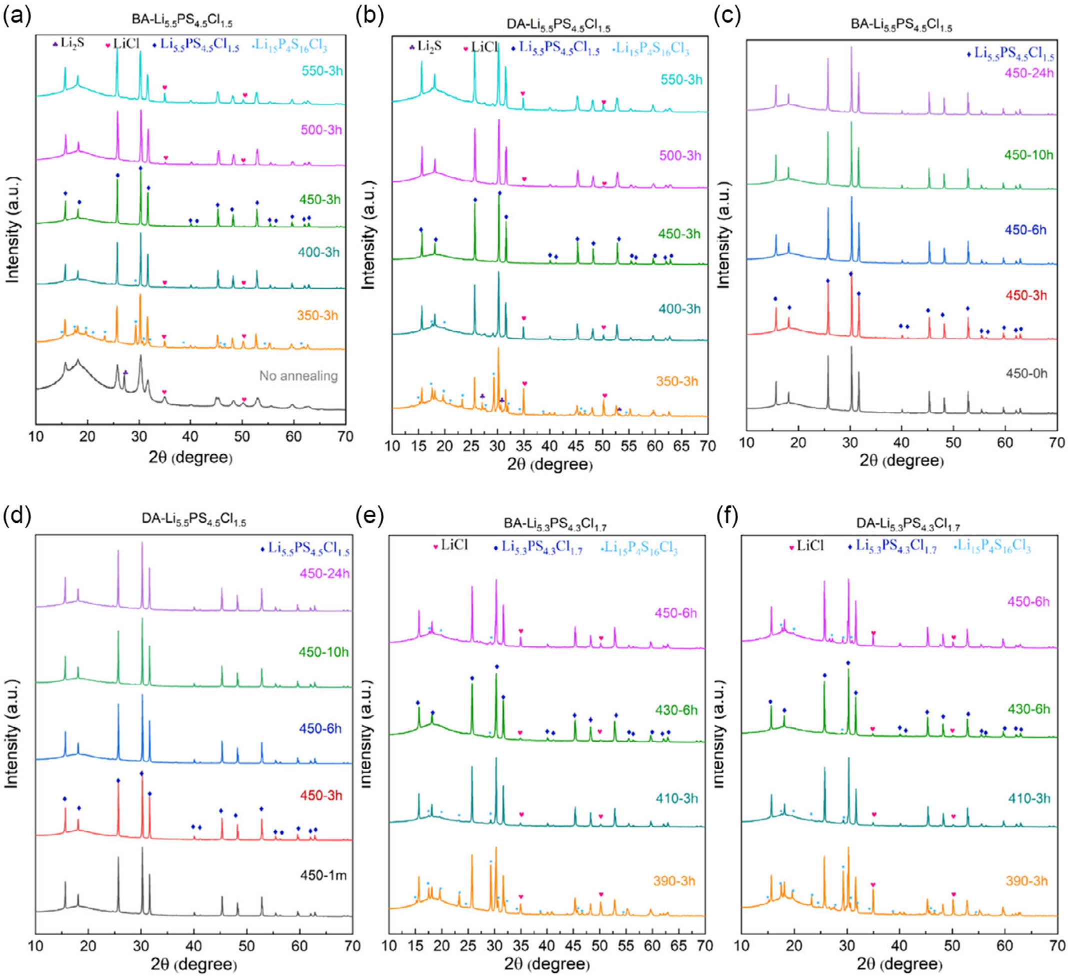

Figure 2. XRD patterns of the BA-$Li_{5.5}PS_{4.5}Cl_{1.5}$ and DA-$Li_{5.5}PS_{4.5}Cl_{1.5}$ samples annealed a,b) at different temperature for 3 h and c,d) at 450 °C for different durations, respectively. XRD patterns of the e) BA-$Li_{5.3}PS_{4.3}Cl_{1.7}$ and f) DA-$Li_{5.3}PS_{4.3}Cl_{1.7}$ samples annealed at different temperatures for 6 h.

450 °C, the content of $Li_{15}P_4S_{16}Cl_3$ and LiCl impurities increases again. From the XRD results of the DA-$Li_{5.3}PS_{4.3}Cl_{1.7}$ samples annealed at different temperature for 6 h (Figure 2f, S3 and S4f, Supporting Information), it can be observed that the phase evolution tendency of DA-$Li_{5.3}PS_{4.3}Cl_{1.7}$ samples is similar to that of the BA-$Li_{5.3}PS_{4.3}Cl_{1.7}$ samples. Therefore, 430 °C is the optimal annealing temperature for obtaining $Li_{5.3}PS_{4.3}Cl_{1.7}$ phase for both the BA-$Li_{5.3}PS_{4.3}Cl_{1.7}$ and DA-$Li_{5.3}PS_{4.3}Cl_{1.7}$ samples. It is obvious that the optimal annealing temperature of $Li_{5.3}PS_{4.3}Cl_{1.7}$ samples is lower than that of the $Li_{5.5}PS_{4.5}Cl_{1.5}$ samples, which might be due to the introduction more chlorine in the $Li_{6-x}PS_{5-x}Cl_{1+x}$ structure.

Furthermore, X-ray photoelectron spectroscopy (XPS) was also conducted to identify the structural evolution of $Li_{5.5}PS_{4.5}Cl_{1.5}$ (see Figure 5 and 6). It can be observed that the XPS of BA-$Li_{5.5}PS_{4.5}Cl_{1.5}$ and DA-$Li_{5.5}PS_{4.5}Cl_{1.5}$ samples synthesized via different annealing temperatures are similar. Owing to subtle difference of Cl between $Li_{5.5}PS_{4.5}Cl_{1.5}$ and LiCl, it is hard to distinguish whether there is LiCl impurity in the $Li_{5.5}PS_{4.5}Cl_{1.5}$ from XPS. In addition, the lines at 161.7 eV in the S 2*p* region and at 132.1 eV in the P 2*p* region represent the PS_4^{3-} group (P—S—Li bond),[25–27] which may originate from $Li_{5.5}PS_{4.5}Cl_{1.5}$ high-conductive phase or $Li_{15}P_4S_{16}Cl_3$ impurity phase (low-conductive phase).

To get further information of the structural evolution of the chlorine-rich lithium argyrodites, **Figure 3**a shows the Raman spectra of the BA-$Li_{5.5}PS_{4.5}Cl_{1.5}$ samples annealed at different temperatures for 3 h. As for the ball-milled sample without annealing, the main peak at 426 cm^{-1} and minor peaks at 196, 262, 576, and 601 cm^{-1} correspond to the PS_4^{3-} group in $Li_{5.5}PS_{4.5}Cl_{1.5}$ phase,[28,29] and the minor peak at 494 cm^{-1} is attributed to S—S bond in the amorphous Li_2S_x phase.[30] While as for the 350-3h samples, beyond $Li_{5.5}PS_{4.5}Cl_{1.5}$ and Li_2S_x from the 350-3h-2 spectra, other peaks at 168 and 240 cm^{-1} from the 350-3h-1 spectra attributed to the PS_4^{3-} group in $Li_{15}P_4S_{16}Cl_3$ phase are also detected. It is found that two different Raman curves exist, which come from different positions of the same 350-3h sample, indicating that the 350-3h sample contains high-conductive $Li_{5.5}PS_{4.5}Cl_{1.5}$ phase and $Li_{15}P_4S_{16}Cl_3$ impurity. With the annealing temperature increasing, the intensities of the peaks corresponding to $Li_{15}P_4S_{16}Cl_3$ and Li_2S_x decrease and finally fade at 450 °C. From 450 to 550 °C, only

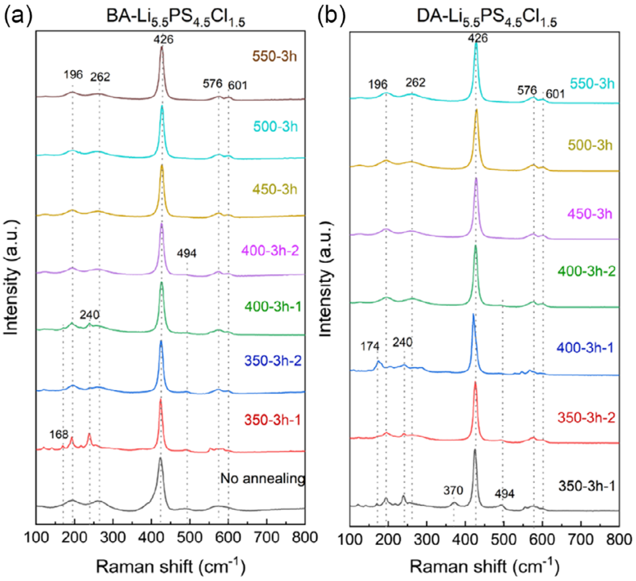

Figure 3. Raman spectra of the a) BA-$Li_{5.5}PS_{4.5}Cl_{1.5}$ and b) DA-$Li_{5.5}PS_{4.5}Cl_{1.5}$ samples annealed at different temperature (350, 400, 450, 500, and 550 °C) for 3 h, respectively.

$PS_4{}^{3-}$ peaks from $Li_{5.5}PS_{4.5}Cl_{1.5}$ show up. From the Raman results of the DA-$Li_{5.5}PS_{4.5}Cl_{1.5}$ samples annealed at different temperature for 3 h (Figure 3b), it is noteworthy that the structural evolution tendency of DA-$Li_{5.5}PS_{4.5}Cl_{1.5}$ samples is similar to that of the BA-$Li_{5.5}PS_{4.5}Cl_{1.5}$ samples. Theses Raman results are in good agreement with XRD results.

Figure S7a, Supporting Information, shows the Raman spectra of the BA-$Li_{5.3}PS_{4.3}Cl_{1.7}$ samples annealing at different temperatures for 6 h. As for the 390-6h samples, apart from the $PS_4{}^{3-}$ group in $Li_{5.3}PS_{4.3}Cl_{1.7}$ phase, the peaks from $Li_{15}P_4S_{16}Cl_3$ phase and amorphous Li_2S_x are also detected. With the annealing temperature increasing, the peaks corresponding to $Li_{15}P_4S_{16}Cl_3$ and Li_2S_x decrease and finally fade at 430 °C. Further increasing the annealing temperature to 450 °C, the peaks corresponding to $Li_{15}P_4S_{16}Cl_3$ reappear. Similar evolution tendency of the structure is also observed in DA-$Li_{5.3}PS_{4.3}Cl_{1.7}$ samples (Figure S7b, Supporting Information).

The Nyquist plots of the BA-$Li_{5.5}PS_{4.5}Cl_{1.5}$, DA-$Li_{5.5}PS_{4.5}Cl_{1.5}$, BA-$Li_{5.3}PS_{4.3}Cl_{1.7}$, and DA-$Li_{5.3}PS_{4.3}Cl_{1.7}$ samples synthesized under different annealing conditions are shown in Figure S8, Supporting Information. All the samples show the only the tail line without any obvious semicircle; therefore, it is not capable to distinguish the grain boundary and bulk resistance of the SEs. The ionic conductivity of these samples was calculated based on the impedance fitting results. The ionic conductivity of BA-$Li_{5.5}PS_{4.5}Cl_{1.5}$ as a function of annealing temperature is shown in **Figure** 4a. The ionic conductivity of the BA-$Li_{5.5}PS_{4.5}Cl_{1.5}$ sample without annealing is 0.85 mS cm^{-1}. After further annealing at 350 °C, the ionic conductivity increases to 1.2 mS cm^{-1}. As the temperature increases, the ionic conductivity continues to increase and reaches maximum at 450 °C and then declines. From 350 to 450 °C, the increase of ionic conductivity is due to the decrease of the $Li_{15}P_4S_{16}Cl_3$, LiCl, and Li_2S impurities.[19,24] The 450-3h sample exhibits the highest ionic conductivity of 8.3 mS cm^{-1}. From 450 to 550 °C, the drop of ionic conductivity is owing to the reappearance and aggregation of LiCl impurities. Therefore, the optimal synthesis temperature is 450 °C. Similar change tendency of ionic conductivity is also found in DA-$Li_{5.5}PS_{4.5}Cl_{1.5}$ electrolytes (Figure 4a). The optimal annealing temperature for the DA-$Li_{5.5}PS_{4.5}Cl_{1.5}$ electrolytes is also 450 °C, which is in accordance with the XRD and Raman results. In addition, a similar ionic conductivity of 8.4 mS cm^{-1} is also achieved in DA-$Li_{5.5}PS_{4.5}Cl_{1.5}$ electrolytes compared with BA-$Li_{5.5}PS_{4.5}Cl_{1.5}$ electrolytes.

The Arrhenius plots of the $Li_{5.5}PS_{4.5}Cl_{1.5}$ samples annealed at different temperatures are shown in Figure S9, Supporting Information. The activation energy E_a is calculated from the slope of the Arrhenius plots according to the Arrhenius equation $\sigma_{ion}T = \sigma_0 \exp(-E_a/k_B T)$, where σ_{ion} is the ionic conductivity of the SE, σ_0 is a pre-exponential factor, T is the absolute temperature, and k_B is the Boltzmann constant.[5] It is noteworthy that the activation energy follows correlation with ionic conductivity (Figure 4a); as the lithium migration pathway energy decreases, lithium-ion mobility increases in intercage jump,[18] resulting in higher ionic conductivity. As for the ball-milled $Li_{5.5}PS_{4.5}Cl_{1.5}$ sample without annealing, the activation energy is about 0.393 eV. After annealing at 350 °C, the activation energy decreases to 0.385 eV. As temperature increases, the activation energy continues to decrease and reaches minimum of 0.318 eV at 450 °C. With further increase in temperature to 550 °C, the activation energy increases to 0.346 eV. Similar change tendency of activation energy is also found in DA-$Li_{5.5}PS_{4.5}Cl_{1.5}$ electrolytes (Figure 4a). The DA-$Li_{5.5}PS_{4.5}Cl_{1.5}$ electrolyte annealing at 450 °C also shows lowest activation energy of 0.32 eV.

Figure 4b shows ionic conductivity of BA-$Li_{5.5}PS_{4.5}Cl_{1.5}$ and DA-$Li_{5.5}PS_{4.5}Cl_{1.5}$ as a function of annealing duration. The ionic conductivity of BA-450-1m sample is 7.4 mS cm^{-1}. As the duration increases, the ionic conductivity of the BA-$Li_{5.5}PS_{4.5}Cl_{1.5}$ sample increases slowly, reaches maximum of 8.5 mS cm^{-1} at 10 h, and then drops to 7.8 mS cm^{-1} at 24 h. It is evident that the ionic conductivity changes slightly when the duration is in the range of 3–10 h. A similar phenomenon is also observed in the DA-$Li_{5.5}PS_{4.5}Cl_{1.5}$ electrolytes.

Figure 4c shows the ionic conductivity of BA-$Li_{5.3}PS_{4.3}Cl_{1.7}$ and DA-$Li_{5.3}PS_{4.3}Cl_{1.7}$ as a function of annealing temperature. As for the BA-390-6 h sample, the ionic conductivity is 1.1 mS cm^{-1}. With the temperature increasing, the ionic conductivity increases quickly, then slowly and reaches maximum of 7.0 mS cm^{-1} at 430 °C, and then declines to 3.4 mS cm^{-1} at 450 °C. Hence, the optimal annealing temperature for the BA-$Li_{5.3}PS_{4.3}Cl_{1.7}$ electrolytes is 430 °C. For the DA-$Li_{5.3}PS_{4.3}Cl_{1.7}$ electrolytes, the change tendency of ionic conductivity is similar to that of the BA-$Li_{5.3}PS_{4.3}Cl_{1.7}$ electrolytes. The DA-$Li_{5.3}PS_{4.3}Cl_{1.7}$ also exhibits highest ionic conductivity of 6.8 mS cm^{-1} at 430 °C, which is comparable to the BA-$Li_{5.3}PS_{4.3}Cl_{1.7}$-430-6h sample. Compared with the $Li_{5.5}PS_{4.5}Cl_{1.5}$-450-3h samples, the ionic conductivity of $Li_{5.3}PS_{4.3}Cl_{1.7}$-430-6h is relatively lower, which is due to the LiCl impurity with low ionic conductivity in the $Li_{5.3}PS_{4.3}Cl_{1.7}$ samples. In addition, the activation energy of the BA-430-6h (0.33 ± 0.04 eV) and DA-430-6h (0.34 ± 0.05 eV) for $Li_{5.3}PS_{4.3}Cl_{1.7}$ (calculated based on Figure 4d) is slightly higher

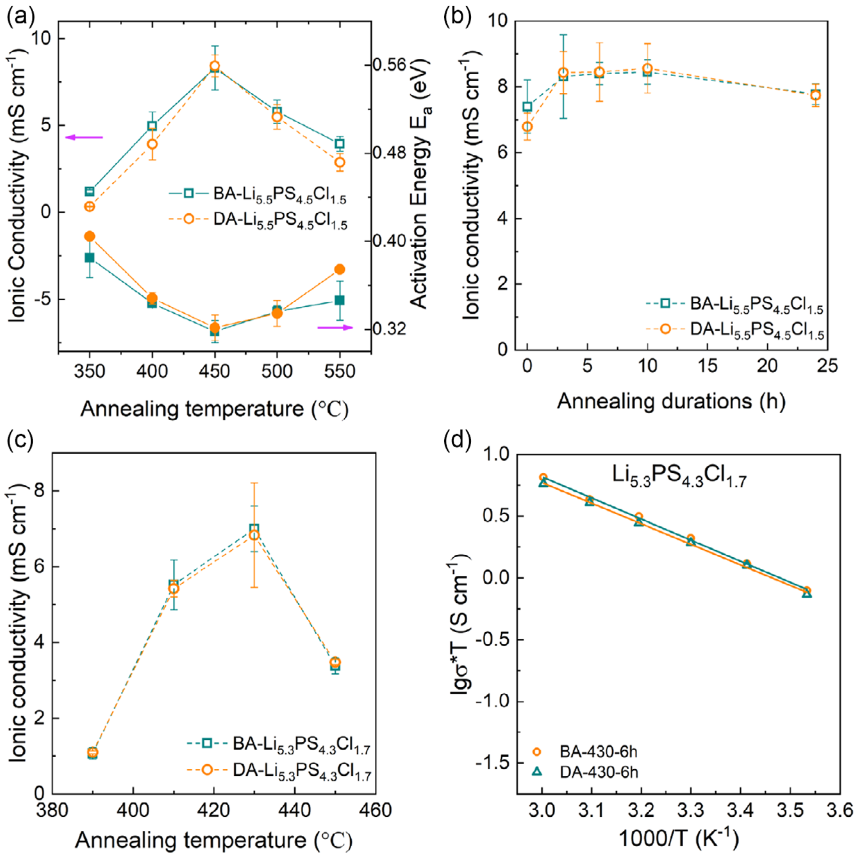

Figure 4. a) Ionic conductivity and activation energy of BA-$Li_{5.5}PS_{4.5}Cl_{1.5}$ and DA-$Li_{5.5}PS_{4.5}Cl_{1.5}$ as a function of annealing temperature, b) ionic conductivity of BA-$Li_{5.5}PS_{4.5}Cl_{1.5}$ and DA-$Li_{5.5}PS_{4.5}Cl_{1.5}$ as a function of annealing durations, c) ionic conductivity of BA-$Li_{5.3}PS_{4.3}Cl_{1.7}$ and DA-$Li_{5.3}PS_{4.3}Cl_{1.7}$ as a function of annealing temperature, and d) Arrhenius plots of the BA-$Li_{5.3}PS_{4.3}Cl_{1.7}$ and DA-$Li_{5.3}PS_{4.3}Cl_{1.7}$ samples annealed at 430 °C for 6 h.

than that of the 450-3h samples for $Li_{5.5}PS_{4.5}Cl_{1.5}$, which could also account for lower ionic conductivity of $Li_{5.3}PS_{4.3}Cl_{1.7}$ compared with $Li_{5.5}PS_{4.5}Cl_{1.5}$.

Comparing the BA samples and DA samples in two SE systems (BA-$Li_{5.5}PS_{4.5}Cl_{1.5}$ vs. DA-$Li_{5.5}PS_{4.5}Cl_{1.5}$; BA-$Li_{5.3}PS_{4.3}Cl_{1.7}$ vs. DA-$Li_{5.3}PS_{4.3}Cl_{1.7}$), the ionic conductivity and activation are quite similar, indicating that a high ionic conductivity with low activation energy for the chlorine-rich lithium argyrodite could be achieved without high-energy ball milling, which would save energy and increase the productivity.

The DC polarization results are shown in Figure S10, Supporting Information. It could be found that the electronic conductivity of BA-$Li_{5.5}PS_{4.5}Cl_{1.5}$ sample ($(7.5 \pm 3) \times 10^{-10}$ S cm^{-1}) is comparable to the DA-$Li_{5.5}PS_{4.5}Cl_{1.5}$ samples ($(9.6 \pm 4) \times 10^{-10}$ S cm^{-1}), demonstrating that $Li_{5.5}PS_{4.5}Cl_{1.5}$ is a pure ionic conductor with a transfer number close to 1.[16]

Figure 5 shows the scanning electron microscopy (SEM) image of the (a) BA-$Li_{5.5}PS_{4.5}Cl_{1.5}$-450-3h sample and corresponding energy dispersive X-ray (EDX) mappings of (b) sulfur and (c) phosphorus and (d) chlorine element. The S, P, Cl elements are distributed uniformly, indicating that homogeneous $Li_{5.5}PS_{4.5}Cl_{1.5}$ SE is obtained. From SEM images of all the $Li_{5.5}PS_{4.5}Cl_{1.5}$ and $Li_{5.3}PS_{4.3}Cl_{1.7}$ electrolytes synthesized via various routes (Figure S11–S14, Supporting Information), the particle size distribution of all the samples is from several hundreds of nm to 20 μm.

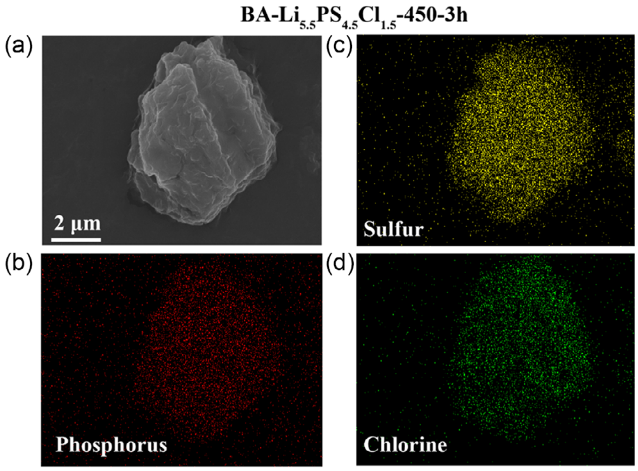

Figure 5. SEM images of the a) BA-$Li_{5.5}PS_{4.5}Cl_{1.5}$-450-3h sample and corresponding b) sulfur and c) phosphorus and d) chlorine EDX mappings.

In order to evaluate the effect of $Li_{5.5}PS_{4.5}Cl_{1.5}$ used in ASSB, the cell with s-NCM83(coated)/$Li_{5.5}PS_{4.5}Cl_{1.5}$ as composite

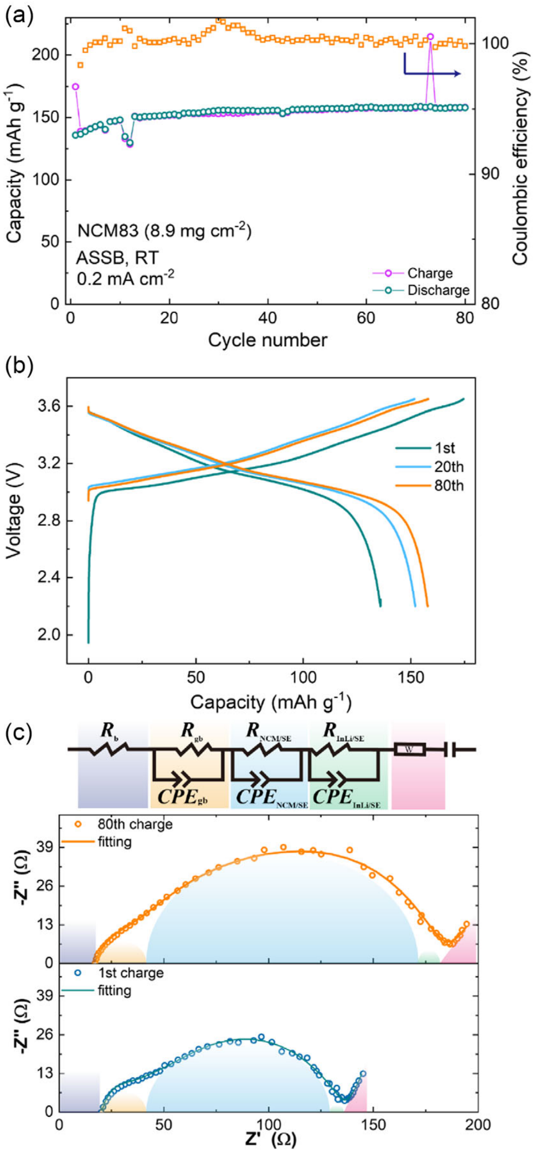

Figure 6. Cycling performance of the In/InLi | $Li_{5.5}PS_{4.5}Cl_{1.5}$ | s-NCM83(coated)- $Li_{5.5}PS_{4.5}Cl_{1.5}$ ASSBs at 0.2 mA cm^{-2} under RT and b) the corresponding discharge–charge voltage profiles of the cells at different cycles. c) Nyquist plots of the cell after 1st and 80th charge and corresponding fitting plots.

cathode, $Li_{5.5}PS_{4.5}Cl_{1.5}$ as electrolyte, and In/InLi as anode was assembled. **Figure 6**a shows the cycling performance of the In/InLi | $Li_{5.5}PS_{4.5}Cl_{1.5}$ | s-NCM83(coated)-$Li_{5.5}PS_{4.5}Cl_{1.5}$ with active material loading of 8.9 mg cm^{-2} at room temperature (RT). The cell delivers an initial discharge capacity of 135 mAh g^{-1} with an initial Columbic efficiency of 78% at 0.2 mA cm^{-2}. Then, the discharge capacity increases and stabilizes at 158 mAh g^{-1} after 80 cycles without any capacity degradation. Such an increase of discharge capacity is due to the activation process of s-NCM83(coated). In particular, the Coulombic efficiency increases to over 99.8% after initial several cycles, indicating superior reversibility of the electrochemical reaction of s-NCM83. In addition, a slight increase of overpotential is observed in the ASSB (see Figure 6b), accounting for good cycling stability of the cell.

To deeply understand the impedance evolution of the ASSB, in situ impedance measurements were conducted on the whole cell after different cycles. Figure 6c shows the Nyquist plots, equivalent circuit, and corresponding fitting plots of the cell after 1st and 80th charge. In the equivalent circuit, the value of R_b is derived from the bulk resistance of $Li_{5.5}PS_{4.5}Cl_{1.5}$. R_{gb} is attributed to the ionic transport resistance of $Li_{5.5}PS_{4.5}Cl_{1.5}$ in the composite cathode, $R_{NCM/SE}$ arises from the interfacial resistance between s-NCM83(coated) and $Li_{5.5}PS_{4.5}Cl_{1.5}$, $R_{InLi/SE}$ originates from the LiIn/SE interfacial resistance, and W stems from the solid-state diffusion of Li^+ in the s-NCM83 particles. After 80 cycles, the value of R_b decreases slightly from 20 to 16.6 Ω, which is attributed to the densification of $Li_{5.5}PS_{4.5}Cl_{1.5}$ during cycling. Compared with slight increase of R_{gb} and $R_{InLi/SE}$, the value of $R_{NCM/SE}$ increases a lot from 87.6 to 131.4 Ω, indicating that the increase of total interfacial resistance is mainly from the $Li_{5.5}PS_{4.5}Cl_{1.5}$/s-NCM83(coated) interface. In addition, the impedance of whole cell does not change obviously after ten cycles (Figure S15, Supporting Information), which could account for high-capacity retention of the ASSB.

3. Conclusion

In summary, we have systematically investigated the evolution of structure, ionic conductivity, and activation energy of chlorine-rich lithium argyrodites (e.g., $Li_{5.5}PS_{4.5}Cl_{1.5}$, $Li_{5.3}PS_{4.3}Cl_{1.7}$) synthesized without/with high-energy ball milling, at various annealing temperature and durations. We found that the ionic conductivity of $Li_{5.5}PS_{4.5}Cl_{1.5}$ and $Li_{5.3}PS_{4.3}Cl_{1.7}$ SEs prepared via fast dry mixing followed by annealing is comparable to those of the electrolytes synthesized via high-energy ball milling.

A high ionic conductivity of 8.3 mS cm^{-1} with low activation energy of 0.32 eV is obtained in the $Li_{5.5}PS_{4.5}Cl_{1.5}$ samples prepared via fast dry mixing followed by annealing at 450 °C for 3 h. Compared with $Li_{5.5}PS_{4.5}Cl_{1.5}$, the optimal annealing temperature is lower for the $Li_{5.3}PS_{4.3}Cl_{1.7}$ with lower ionic conductivity of 7.0 mS cm^{-1}. In addition, ASSB with s-NCM83(coated) and $Li_{5.5}PS_{4.5}Cl_{1.5}$ as cathode, $Li_{5.5}PS_{4.5}Cl_{1.5}$ as solid electrolyte, and In/InLi as anode offer a stable capacity of 158 mAh g^{-2} at 0.2 mA cm^{-2} after 80 cycles, demonstrating that chlorine-rich lithium argyrodite is a promising candidate for ASSBs. Our work deepens the understanding of the effect of processing on the structure and ionic conductivity of the chlorine-rich lithium argyrodites.

4. Experimental Section

Solid Electrolyte Synthesis: The starting materials LiCl (Aladdin, 99%), P_2S_5 (Sigma-Aldrich, 99%) and Li_2S (Alfa, 99.9%) were weighed in an appropriate ratio. For the BA-$Li_{5.5}PS_{4.5}Cl_{1.5}$ SEs, the precursor was ball milled using a planetary ball milling apparatus (Fritsch Pulverisette 7 Premium) at 520 rpm for 48 cycles of each 20 min milling and 10 min break. Then the as-milled material was pressed into pellets and sealed in vacuum quartz ampoules. After that, the ball-milled mixture was annealed at 350, 400, 450, 500, and 550 °C for 3 h, respectively. The samples annealed at various temperature were denoted as 350-3h, 400-3h, 450-3h, 500-3h, and 550-3h, respectively. While for the BA-$Li_{5.3}PS_{4.3}Cl_{1.7}$

electrolytes, the ball-milled mixture was annealed at 390, 410, 430, and 450 °C for 6 h, respectively, which was named as 390-6h, 410-6h, 430-6h, and 450-6h, respectively. After the annealing temperature was optimized, the annealing durations were tuned to obtain the optimal durations. For example, the ball-milled samples were annealed at 450 °C for 1 min, 3, 6, 10, 24 h, respectively, which were denoted as 450-1m, 450-3h, 450-6h, 450-10h, and 450-24h, respectively. The tubes were cooled down to RT naturally in the furnace.

For the DA-$Li_{5.5}PS_{4.5}Cl_{1.5}$ and DA-$Li_{5.3}PS_{4.3}Cl_{1.7}$ SEs, the precursor was mixed using a pulverizer with a rotation speed of 18 000 rpm for 3 min, and then the premixed powders were annealed. The annealing process for the DA-$Li_{5.5}PS_{4.5}Cl_{1.5}$ samples was similar to the above BA-$Li_{5.5}PS_{4.5}Cl_{1.5}$ samples. In addition, the annealing process for the DA-$Li_{5.3}PS_{4.3}Cl_{1.7}$ samples was similar to the above BA-$Li_{5.3}PS_{4.3}Cl_{1.7}$ samples.

Characterization: The XRD patterns were collected using a diffractometer (D8 Advance, Bruker) equipped with a Cu Kα radiation source to identify the phase of SEs. The XRD data was collected with 2θ from 10° to 90° at a scan rate of $1° \min^{-1}$. The samples were kept in a home-made container covered by a Kapton polyimide film to prevent side reaction with moisture and oxygen. The TOPAS-Academic V6 software package was used to perform Rietveld refinements. More details could be found in the previous work.[18] Raman spectra were obtained via using a Raman spectrometer (LabRAM HR Evolution, Horiba) at an excitation of 532 nm. The samples were sealed in a home-made chamber covered with a quartz glass window in the glovebox.

The XPS experiments were carried out on the surface of solid electrolyte pellets using an XPS spectrometer (PHI 5300, Perkin Elmer) with a monochromatized Al *K*α source (1486.6 eV). The sample surface was cleaned via Ar^+ sputtering with an acceleration voltage of 2 kV for 180 s. The particle and pellet morphology of the SEs was obtained by SEM (SEM, Zeiss Merlin) at an acceleration voltage of 15 kV together with energy-dispersive X-ray spectroscopy.

Electrochemical Measurements: To obtain the ionic conductivity of the SEs, 120 mg of the SE powder was pressed into pellet with a diagram of 12 mm under 150 MPa. Two stainless steel rods were attached to the pellet as current collectors. The AC impedance measurements were conducted using an impedance analyzer (ZAHNER, Zennium Pro) in the frequency range of 8 MHz–1 Hz with an amplitude of 50 mV at RT. For the activation energy tests, the impedance data were collected in the temperature range of 10−60 °C. For electronic conductivity measurements, 150 mg of the SE powder was pressed into a pellet with a diagram of 10 mm under 150 MPa. Two stainless steel disks were used as current collectors. The DC polarization tests were performed with applied constant voltages of 0.2, 0.4, 0.6, 0.8, and 1.0 V for 6 h, respectively.

Cell Assembly and Test: The In/InLi | $Li_{5.5}PS_{4.5}Cl_{1.5}$ | s-NCM83(coated)-$Li_{5.5}PS_{4.5}Cl_{1.5}$ ASSB cells were fabricated for the galvanostatic cycling tests. The s-NCM83(coated) (provided from BASF shanshan Battery Materials Co. Ltd.) was hand ground with $Li_{5.5}PS_{4.5}Cl_{1.5}$ in a weight ratio of 70:30 for 30 min to obtain the s-NCM83(coated)-$Li_{5.5}PS_{4.5}Cl_{1.5}$ composite cathode. Detailed assembly process was as follows. First, 80 mg of $Li_{5.5}PS_{4.5}Cl_{1.5}$ powder was pressed in a poly(ether-ether-ketone) model under 100 MPa with a diameter of 10 mm. Then, 7 mg of the composite cathode was spread uniformly onto one side of the solid electrolyte layer and pressed under 50 MPa. After that, an indium foil and a lithium foil were attached to another side of solid electrolyte layer and then pressed under 100 MPa. Finally, the whole cell was pressed under 150 MPa for 3 min. The cells were tested in a homemade cell at a constant pressure of ≈100 MPa at RT using VMP-3 Biologic potentiostat/galvanostat in a voltage range of 2.2−3.65 V (vs. In/InLi), corresponding to 2.8−4.25 V (vs. Li^+/Li). The in situ impedance of the cells after cycling was measured using a VMP-3 Biologic in the frequency range from 1 MHz to 3 mHz at RT. All the assembly and test procedures were conducted under Ar atmosphere in a glovebox ($[O_2] < 0.1$ ppm, $[H_2O] < 0.1$ ppm).

Supporting Information

Supporting Information is available from the Wiley Online Library or from the author.

Acknowledgements

This work was supported by Basic Science Center Program of National Natural Science Foundation of China under grant no. 51788104, the Fundamental Research Funds for the Central Universities (WUT: 2022IVA005), and Guangdong Basic and Applied Basic Research Foundation (grant no. 2021A1515110312). The authors thank Xinxin Tan for providing the s-NCM83-(coated) cathode.

Conflict of Interest

The authors declare no conflict of interest.

Data Availability Statement

The data that support the findings of this study are available in the supplementary material of this article.

Keywords

$Li_{5.5}PS_{4.5}Cl_{1.5}$, lithium argyrodites, solid-state batteries, solid-state reactions, sulfide solid electrolytes

Received: December 4, 2022
Revised: January 20, 2023
Published online: February 5, 2023

---

[1] S. Randau, D. A. Weber, O. Kötz, R. Koerver, P. Braun, A. Weber, E. Ivers-Tiffée, T. Adermann, J. Kulisch, W. G. Zeier, F. H. Richter, J. Janek, *Nat. Energy* **2020**, *5*, 259.

[2] F. Strauss, D. Kitsche, Y. Ma, J. H. Teo, D. Goonetilleke, J. Janek, M. Bianchini, T. Brezesinski, *Adv. Energy Sustainability Res.* **2021**, *2*, 2100004.

[3] X. Miao, S. Guan, C. Ma, L. Li, C. W. Nan, *Adv. Mater.* **2022**, 2206402, https://doi.org/10.1002/adma.202206402.

[4] A. Bielefeld, D. A. Weber, J. Janek, *ACS Appl. Mater. Interfaces* **2020**, *12*, 12821.

[5] S. Ohno, A. Banik, G. F. Dewald, M. A. Kraft, T. Krauskopf, N. Minafra, P. Till, M. Weiss, W. G. Zeier, *Prog. Energy* **2020**, *2*, 022001.

[6] S. Wang, X. Wu, Y. Liang, Y. Xu, S. Guan, K. Wen, X. Miao, Y. Liang, H. He, Y. Lin, Y. Shen, C.-W. Nan, *Front. Chem. Eng.* **2022**, *4*, 883502.

[7] M. A. Kraft, S. Ohno, T. Zinkevich, R. Koerver, S. P. Culver, T. Fuchs, A. Senyshyn, S. Indris, B. J. Morgan, W. G. Zeier, *J. Am. Chem. Soc.* **2018**, *140*, 16330.

[8] N. Kamaya, K. Homma, Y. Yamakawa, M. Hirayama, R. Kanno, M. Yonemura, T. Kamiyama, Y. Kato, S. Hama, K. Kawamoto, A. Mitsui, *Nat. Mater.* **2011**, *10*, 682.

[9] L. Zhou, A. Assoud, Q. Zhang, X. Wu, L. F. Nazar, *J. Am. Chem. Soc.* **2019**, *141*, 19002.

[10] S. Wang, R. Fang, Y. Li, Y. Liu, C. Xin, F. H. Richter, C.-W. Nan, *J. Materiomics* **2021**, *7*, 209.

[11] X. Chen, J. Xie, X. Zhao, T. Zhu, *Adv. Energy Sustainability Res.* **2021**, *2*, 2000101.

[12] L. Zhou, N. Minafra, W. G. Zeier, L. F. Nazar, *Acc. Chem. Res.* **2021**, *54*, 2717.

[13] J. Ruhl, L. M. Riegger, M. Ghidiu, W. G. Zeier, *Adv. Energy Sustainability Res.* **2021**, *2*, 2000077.

[14] S. Wang, Y. Zhang, X. Zhang, T. Liu, Y. H. Lin, Y. Shen, L. Li, C. W. Nan, *ACS Appl. Mater. Interfaces* **2018**, *10*, 42279.

[15] N. J. J. de Klerk, I. Rosłoń, M. Wagemaker, *Chem. Mater.* **2016**, *28*, 7955.

[16] P. Adeli, J. D. Bazak, K. H. Park, I. Kochetkov, A. Huq, G. R. Goward, L. F. Nazar, *Angew. Chem., Int. Ed.* **2019**, *58*, 8681.

[17] W. D. Jung, J. S. Kim, S. Choi, S. Kim, M. Jeon, H. G. Jung, K. Y. Chung, J. H. Lee, B. K. Kim, J. H. Lee, H. Kim, *Nano Lett.* **2020**, *20*, 2303.

[18] A. Gautam, M. Ghidiu, E. Suard, M. A. Kraft, W. G. Zeier, *ACS Appl. Energy Mater.* **2021**, *4*, 7309.

[19] Y. Liu, H. Su, Y. Zhong, X. Wang, X. Xia, C. Gu, J. Tu, *Adv. Funct. Mater.* **2022**, *32*, 2207978.

[20] L. Peng, H. Ren, J. Zhang, S. Chen, C. Yu, X. Miao, Z. Zhang, Z. He, M. Yu, L. Zhang, S. Cheng, J. Xie, *Energy Storage Mater.* **2021**, *43*, 53.

[21] C. Yu, Y. Li, M. Willans, Y. Zhao, K. R. Adair, F. Zhao, W. Li, S. Deng, J. Liang, M. N. Banis, R. Li, H. Huang, L. Zhang, R. Yang, S. Lu, Y. Huang, X. Sun, *Nano Energy* **2020**, *69*, 104396.

[22] X. Feng, P.-H. Chien, Y. Wang, S. Patel, P. Wang, H. Liu, M. Immediato-Scuotto, Y.-Y. Hu, *Energy Storage Mater.* **2020**, *30*, 67.

[23] L. Peng, C. Yu, Z. Zhang, H. Ren, J. Zhang, Z. He, M. Yu, L. Zhang, S. Cheng, J. Xie, *Chem. Eng. J.* **2022**, *430*, 132896.

[24] Z. Liu, T. Zinkevich, S. Indris, X. He, J. Liu, W. Xu, J. Bai, S. Xiong, Y. Mo, H. Chen, *Inorg. Chem.* **2020**, *59*, 226.

[25] S. Wang, M. Tang, Q. Zhang, B. Li, S. Ohno, F. Walther, R. Pan, X. Xu, C. Xin, W. Zhang, L. Li, Y. Shen, F. H. Richter, J. Janek, C. W. Nan, *Adv. Energy Mater.* **2021**, *11*, 2101370.

[26] S. Wang, W. Zhang, X. Chen, D. Das, R. Ruess, A. Gautam, F. Walther, S. Ohno, R. Koerver, Q. Zhang, W. G. Zeier, F. H. Richter, C. W. Nan, J. Janek, *Adv. Energy Mater.* **2021**, *11*, 2100654.

[27] T. T. Zuo, F. Walther, J. H. Teo, R. Ruess, Y. Wang, M. Rohnke, D. Schroder, L. F. Nazar, J. Janek, *Angew. Chem., Int. Ed.* **2023**, e202213228.

[28] Y. Zhou, C. Doerrer, J. Kasemchainan, P. G. Bruce, M. Pasta, L. J. Hardwick, *Batteries Supercaps* **2020**, *3*, 647.

[29] C. Dietrich, D. A. Weber, S. Culver, A. Senyshyn, S. J. Sedlmaier, S. Indris, J. Janek, W. G. Zeier, *Inorg. Chem.* **2017**, *56*, 6681.

[30] L. Sang, R. T. Haasch, A. A. Gewirth, R. G. Nuzzo, *Chem. Mater.* **2017**, *29*, 3029.